Acta metall. mater. Vol. 41, No. 9, pp. 2533–2546, 1993
Printed in Great Britain.

0956-7151/93 $6.00 + 0.00

SEGREGATION TO AND STRUCTURE OF [001] TWIST GRAIN BOUNDARIES IN Cu–Ni ALLOYS

H. Y. WANG,[1] R. NAJAFABADI,[1] D. J. SROLOVITZ[1] and R. LESAR[2]

[1]Department of Materials Science and Engineering, The University of Michigan, Ann Arbor, MI 48109-2136 and [2]Theoretical Division, Los Alamos National Laboratory, Los Alamos, NM 87545, U.S.A.

(Received 23 October 1992; in revised form 10 March 1993)

Abstract—The segregation, thermodynamic, and structural properties of [001] twist boundaries in Cu–Ni alloys have been examined within a wide range of misorientations and temperatures. Cu always segregates to the boundary. The concentration of the first layer adjacent to the boundary increases monotonically with misorientation and no obvious cusps are observed. All other thermodynamic properties vary smoothly with the misorientation, with the exception of the vibrational entropy of the boundaries without segregation. The unsegregated vibrational entropy shows a large peak at the misorientation corresponding to the $\Sigma 17$ boundary and two minima around the $\Sigma 13$ and $\Sigma 5$ boundary orientations. The concentration distribution within the plane of the grain boundaries can be described by the same structural unit model established for [001] twist boundaries in pure materials. Regions of large tensile stress show greater segregation than do regions of compressive stress. Regions of large shear stress tend to show reduced segregation compared with regions of small shear stress.

1. INTRODUCTION

A large body of experimental and theoretical evidence demonstrates that the properties of grain boundaries vary with their crystallographic orientation and boundary structure [1–8]. While most atomistic simulation studies of grain boundaries were performed at zero temperature owing to their computational simplicity [4], essentially all experimental studies of segregation have been performed at elevated temperature, where segregation kinetics are fast. Although several finite temperature simulation of grain boundaries have been performed using Monte Carlo (MC) and molecular dynamics (MD) [9], most of these studies focused on individual grain boundaries and grain boundary melting [10]. The first systematic study of the misorientation dependence of thermodynamic properties at finite temperature was recently performed by Najafabadi *et al.* [8] using the local harmonic (LH) method to obtain the equilibrium structure and thermodynamics of [001] twist grain boundaries in pure Au. It was observed that first order structural phase transitions occurred at some grain boundaries and small cusps in the energy vs misorientation plots occurred at $\Sigma 5$ and $\Sigma 13$ at low temperatures, at $\Sigma 13$ and $\Sigma 17$ at intermediate temperatures, and at $\Sigma 5$ and $\Sigma 17$ at elevated temperatures. Such systematic finite-temperature studies of grain boundaries are necessary to bridge the gaps between atomistic simulations and experiments performed at elevated temperatures.

Extensive efforts [7, 11–17] have been made to examine the relationship between the structures of various boundaries throughout a misorientation range for a given twist or tilt axis in pure materials. The now standard structural unit model [7, 11–17] for the atomic structure of grain boundaries was developed based upon such systematic simulation investigations. This model describes the structure of all long-period grain boundaries within a certain misorientation range in terms of specific sequences of structural units of certain shorter period boundaries delimiting the misorientation range. If the delimiting boundary unit is not composed of units from other boundaries, it is regarded as a favored boundary according to the definition of Sutton and Vitek [13], and this unit is then a fundamental structural element of nearby boundary structures. For example, Sutton *et al.* [11, 13] found that all $\Sigma \leqslant 491$ symmetrical [1$\bar{1}$0] tilt boundaries in the region between $\Sigma 27$ (115) (31.59°) and $\Sigma 11$ (113) (50.48°) were composed of predictable sequences of units of these two boundaries.

While in the case of [001] twist boundaries, it was found that the structures of all boundaries between 0° and 36.87° ($\Sigma 5$) can be decomposed into units of the ideal crystal and units of the $\Sigma 5$ boundary, and the structure of all boundaries between 36.87° and 45° are composed of different units of the two types of $\Sigma 5$ boundaries [12, 15], a third unit, called a filler unit, is always needed to completely decompose each structure. In terms of the grain boundary dislocations (GBD) description, the structure of a boundary with a misorientation between those of delimiting boundaries can be regarded as the delimiting boundaries with a superimposed network of screw dislocations. Most of the structure between the dislocations can be described in terms of the units of one of the delimiting

boundaries. The intersections of the dislocations give rise to the minority units composed of units of the other delimiting boundary. The core of the dislocations in between these dislocation intersections are centered on rows of filler units.

In the present study, we will also focus on [001] twist boundaries. However, instead of concentrating on the structure of boundaries in pure materials, the present study focuses on the effects of misorientation on grain boundary segregation and thermodynamics, the distribution of the segregant at the boundary and the changes in the grain boundary structure due to segregation. Simulations based upon the LH model (described below) will be performed on ten different [001] twist boundaries in Cu–Ni alloys for temperatures between 600 to 1100 K at a composition of $Ni_{0.95}Cu_{0.05}$. The (001) plane has 4-fold symmetry and hence $0° \leqslant \theta \leqslant 45°$ covers entire misorientation region. The ten [001] twist boundaries examined are listed in Table 1.

Several different methods have been developed for predicting interfacial segregation behavior; including classical analytical theories such as those developed by Langmuir and MacLean [18], zero temperature atomistic simulations (see Ref. [18] and references therein) and Monte Carlo simulations [20, 21]. While the classical theories may work well in some cases in dilute alloys, they do not self-consistently account for the structure of the interface. Although zero-temperature atomistic simulations [18] have been used to determine the segregation energy of each atomic site near a grain boundary, this type of simulation cannot be used to predict the degree of segregation at other than very low solute concentrations due to interactions between solute atoms. Recent developments in Monte Carlo methods have extended atomistic simulations to alloy systems where the local composition may be properly accounted for and allowed to change. This approach has led to truly atomistic studies of equilibrium segregation at interfaces [20–23]. However, this approach requires substantial computational resources and has never been successfully used to obtain finite-temperature segregation thermodynamics, including the free energy of segregation.

We have recently developed [24–29] a simple simulation method that predicts trends in interfacial behavior that has been shown to yield good agreement with accurate Monte Carlo studies of segregation and perfect-crystal thermodynamics [24, 25], and yet is much more computationally efficient. The theory behind the simulation method is based upon a number of simple approximations centered on the concept of effective (or mean-field) atoms that have properties that are a concentration-weighted mix of different atoms types. The central approximations in the model are: (1) the vibrations of the atoms are determined within the framework of the Local Harmonic (LH) model [30] in which the terms in the dynamical matrix that couple vibrations of different atoms are ignored; (2) a mean-field expression for the interaction energy described by embedded-atom method (EAM) potentials [20] for metals; and (3) an ideal-mixing approximation to the configurational entropy [31]. The most important feature of this method is that it yields a simple expression for the finite-temperature free energy of the system. Minimizing the free energy with respect to the positions and concentrations of the atomic sites yields the equilibrium structure and free energy, from which all other thermodynamic quantities can be derived.

In the following section, we briefly summarize the free energy minimization method. In Section 3, we examine the segregation profile. Segregation thermodynamics are analyzed in the following section. The distribution of segregants within the boundary plane, the influence of segregation on the boundary structure, and the validity of the structural unit model in alloys is examined in Section 4. The final sections of this report considers the correlation of segregation sites with atomic level stresses and the influence of segregation upon these stresses.

2. FREE ENERGY SIMULATION METHOD

The free energy simulation method employed in the present study was described in detail in Ref. [24], so in this section, we provide only a brief synopsis. The free energy of an alloy consists of three parts: atomic bonding, atomic vibrations and configurational entropy. We describe the atomic bonding using the embedded-atom method (EAM) potential [20]. The effects of atomic vibrations are included within the framework of the local harmonic (LH) model [30]. The vibrational contribution to the LH free energy within the classical limit is given by

$$A_v = k_B T \sum_{i=1}^{N} \sum_{\beta=1}^{3} \ln\left(\frac{h\omega_{i\beta}}{2\pi k_B T}\right) \tag{1}$$

where $k_B T$ is the thermal energy, h is Planck's constant, N is the total number of atoms in the system, and ω_{i1}, ω_{i2}, and ω_{i3} are the three vibrational eigenfrequencies of atom i. These frequencies may be determined in terms of the local dynamical matrix of each atom $D_{i\alpha\beta} = (\partial^2 E/\partial x_{i\alpha}\partial x_{i\beta})$, where the $x_{i\beta}$ correspond to atomic displacements of atom i in some coordinate system [30].

Table 1. The reciprocal coincident lattice site density Σ corresponding to the different [001] twist misorientations examined in the present study

Σ	25	37	13	89	17	65	53	109	5	73
θ(°)	16.26	18.92	22.67	25.98	28.07	30.51	31.89	33.40	36.87	41.11

Within the point (i.e. Bragg–Williams) [31] approximation, the configurational entropy may be written as

$$S_c = -k_B \sum_{i=1}^{N} \{c_a(i) \ln[c_a(i)] + c_b(i) \ln[c_b(i)]\} \quad (2)$$

where $c_a(i)$ is the concentration of a atoms and $c_b(i)$ is the concentration of b atoms on site i. Since we are interested in equilibrium properties, these concentrations may be viewed as the time averaged composition of each atomic site in a system where the atoms are free to diffuse. In this sense, the atoms are "effective" or "mean-field" atoms. Since we replace real atoms by effective atoms, the internal energy E which is defined in terms of the interatomic potential must also be suitably averaged over the composition of each atom and its interacting neighbors. A method for performing these averages for the EAM potentials is described in Refs [24, 26].

In the simulations described below, we employ a reduced grand canonical ensemble, where the total number of atoms remains fixed but the relative amounts of each atomic species vary. The appropriate thermodynamic potential for this type of ensemble is the Grand potential and is given by [32]

$$\Omega = E + A_v - TS_c - \Delta\mu \sum_{i=1}^{N} c_a(i) \quad (3)$$

where $\Delta\mu$ is the difference in chemical potential between the a and b atoms. Given $\Delta\mu$, the equilibrium concentration at each site may be determined by minimizing Ω with respect to those concentrations. This approach (without the vibrational contributions to the free energy) was previously employed by Lundberg [33] in a restrictive model of surface segregation.

Several approximations were employed in arriving at the expression for the grand potential which we employ. These were primarily the local harmonic model, the Bragg–Williams approximation and the mean field approximation to the energy. The LH model yields quantitative agreement with Monte Carlo [30] and quasiharmonic calculations [36] over a wide range of temperature for perfect crystals and many defects. The Bragg–Williams approximation is known to produce substantial error near phase transitions. However, comparisons with Monte Carlo segregation data using the same interatomic potentials show that in most segregation situations the Bragg–Williams model does not introduce serious errors [24]. We have also compared the EAM energies obtained for solid solution alloys [37] and vacancies [38] using the mean field approximation and discrete atom types and find that the errors for solid solution crystals are negligible and the errors associated with the vacancy formation energy (including short range order in the Cu–Ni system) to be very small.

The calculation of the equilibrium segregation around an interface is performed in steps. First, the properties of the perfect, uniform composition crystal are determined (see Ref. [26]), which is done by choosing a composition, temperature, and pressure and then minimizing the free energy with respect to the lattice parameter. Differentiating the equilibrium free energy with respect to composition yields the chemical potential difference $\Delta\mu$. For the Cu–Ni alloy system, we have verified that the equilibrium structure is a solid solution at the temperature, pressure and composition of interest by minimizing the grand potential [equation (3)] with respect to lattice parameter and local concentration and verifying that the resultant concentration profile was uniform. Since at equilibrium the chemical potential difference is everywhere constant, we fix the chemical potential difference at their bulk values, introduce the appropriate interface, and minimize the Grand potential with respect to the concentration and position of each site.

The geometry of the cell used in the grain-boundary simulations is the same as that employed in earlier studies of grain boundaries in pure systems [34]. The simulation cell is divided into two regions, I and II. The effective atoms in region I are completely free to move in response to the temperature- and concentration-dependent forces ("F_i" $= -\partial\Omega/\partial r_i$) due to other atoms and the concentration at each site is allowed to vary. The atoms in Region II, however, are constrained such that region II is a perfect crystal with the lattice constant and average concentration on each site appropriate to the simulation temperature, pressure, and bulk concentration. The equilibrium configuration and concentrations of the effective atoms are obtained by minimizing equation (3) with respect to atomic coordinates, site concentrations, and the relative positions of the upper and lower crystals ($4N + 3$ variables, where N is the number of atoms in the system).

3. SEGREGATION PROFILE

Following segregation, the concentration profile in the bicrystal is not uniform and the mean (dimensionless) concentration on the (002) planes parallel to the boundary are given by C_n, where the subscript n denotes the plane number [e.g. C_3 is the mean concentration in the third (002) plane from the boundary]. We denote the dimensionless bulk concentration far from the grain boundary plane as C_B. Due to the four fold [001] axis symmetry in these twist boundaries, the number of distinct concentration levels on each (002) plane is $1 + (\Sigma - 1)/4$. However, in the segregation profiles to be shown in the following, the number of distinguishable concentration levels may be less than this number because some of the concentration levels are very close. Throughout this paper, all concentrations $0 \leqslant C \leqslant 1$ will refer to the Cu concentration; the concentration of Ni is given simply by $1 - C$.

The mean Cu concentration on the first layer C_1 as a function of misorientation θ is plotted in Fig. 1(a)

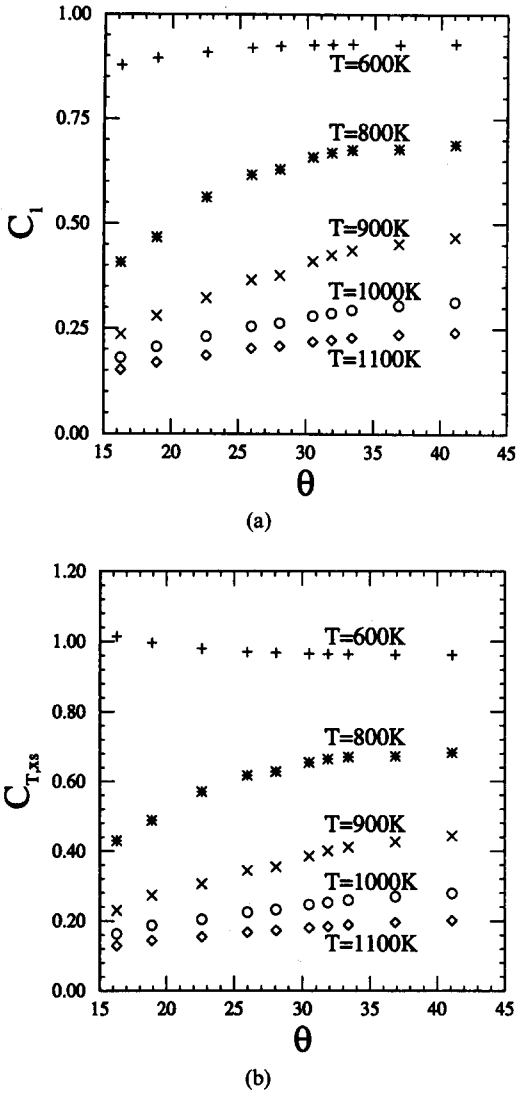

Fig. 1. Concentration of Cu atoms averaged over the first layer C_1 (a) and the total excess concentration of Cu (b) vs the grain boundary misorientation.

for $C_B = 0.05$ at five different temperatures. We note that the heat of segregation can be calculated from the temperature dependence of the layer concentration C_1 [26, 27]. These curves show that Cu always segregates to the grain boundary for all misorientations examined. As the misorientation angle is increased from 0° to 45°, the Cu concentration on the (002) plane adjacent to the boundary increases. This variation of the strength of segregation with misorientation is attributable to the increase density of preferential segregation sites (near dislocations) at the boundary with increasing misorientation (at least for $\theta < 36.87°$, i.e. until the basic structural unit changes at Σ5). No strong cusps in the C_1 vs θ plot are observed anywhere in the entire misorientation range studied. However, very small inflections appear at the Σ5 and Σ17 boundaries at 800 and 900 K. The main effect of increasing temperature is to reduce the magnitude of the Cu segregation for all orientations. At the lowest and highest temperatures examined (600 and 1100 K) the composition vs misorientation curves tend to be relatively flat. This may be understood by considering that at low temperature the Cu segregation is very strong along the entire boundary (i.e. kT is small compared to essentially all of the local heats of segregation) and at very high temperatures entropic effects are sufficiently strong to dominate the enthalpic tendencies for segregation (i.e. kT is large compared to the heat of segregation). Thus, in either case, the boundary concentration will be nearly constant; close to one for low temperature and slightly elevated relative to C_B for high temperature. At intermediate temperatures, the variation in the density of preferential nucleation sites with changes in misorientation causes the strength of the grain boundary segregation to vary with θ.

For the Σ5 boundary in Cu–Ni alloys, the boundary width is only about 2–3 (002) interplanar spacings on each side of the boundary and the segregation to the first layer usually dominates the total segregation [26]. Such behavior is also observed in the boundaries with other misorientations. In Fig. 1(b), we plot the total excess concentration of Cu, $C_{T,xs}$, as a function of the misorientation, where

$$C_{T,xs} = \sum_{n=1}^{\infty} (C_n - C_B).$$

The shape of these curves are quite similar to that of the C_1 curves shown in Fig. 1(a), except that at $T = 600$ K $C_{T,xs}$ initially decays with increasing misorientation. This suggests that when the atomic layer adjacent to the boundary is nearly saturated, the second (002) plane from the boundary may contribute significantly to determine the overall degree of segregation.

4. THERMODYNAMICS

The thermodynamic properties of grain boundaries are distinguished from the bulk properties by the subscripts B or gb, where B represents bulk (solid solution) crystal properties and gb refers to grain boundary properties. The grain boundary properties are defined as the difference between the property of the bicrystal and that of a solid solution with the same number of atoms at the same chemical potential and temperature: $X_{gb} = [X(\text{bicrystal}) - X_B]/A$, where X is the thermodynamic property of interest (e.g. free energy, enthalpy, etc.) and the grain boundary properties have been normalized by the grain boundary area, A. The grain boundary properties may be calculated in two limits. The first is the unsegregated limit, in which the grain boundary is only relaxed with respect to the atomic positions, as may be found by quenching the sample from very high temperature (where segregation is negligible) to the temperature of interest. The second is the segregated limit, which corresponds to equilibrium segregation at the temperature of interest, i.e. the boundary is fully relaxed

with respect to both the atomic positions and the atomic concentrations.

The grain boundary free energy, in the grand canonical ensemble, is denoted as $\Gamma_{gb} = (\Omega_{gb} - \Omega_B)/A$, where Ω_{gb} is the grand potential of the system with the grain boundary, Ω_B is the grand potential for the perfect crystal and the A is the area of the grain boundary. The misorientation dependence of the boundary free energy is shown in Fig. 2. In the unsegregated case [Fig. 2(a)], the boundary free energy increases as the misorientation increases. A very weak inflection is observed at the orientation of the Σ5 boundary 36.87°. As the temperature increases the magnitude of the grain boundary free energy decreases, indicating that the grain boundary has a positive excess entropy [8].

For the fully relaxed boundary [Fig. 2(b)], the variation of the Γ_{gb} curves with T and θ is complicated due to the competition between the various terms that make up the free energy. At low temperatures, the entropy makes a smaller contribution to the free energy, so that Γ_{gb} is larger. However, also at low temperatures, the contribution from the energy that drives segregation is larger and, hence, the magnitude of Γ_{gb} is smaller. The lowest value for the boundary free energy occurs at $T = 600$ K, implying that at this temperature at $C_B = 0.05$, the contribution to the free energy from the segregation dominates the contribution from the entropy. When temperature increases, the grain boundary free energy also tends to increase. However, at $900 \leqslant T(\mathrm{K}) \leqslant 1100$ K, the magnitude of the boundary free energy is nearly independent of temperature. In this temperature range, the competition between the energy-favored segregation and the entropy-driven homogenization is nearly balanced.

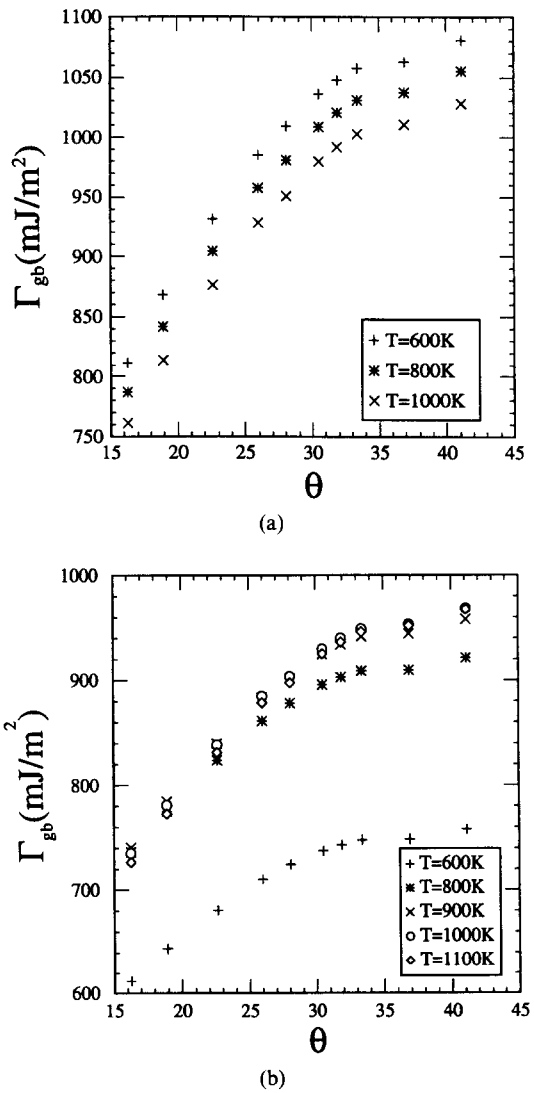

Fig. 2. The grain boundary free energy vs the grain boundary misorientation (a) for the unsegregated boundary and (b) for the segregated boundary.

The boundary entropy may be evaluated as $-(\partial G_{gb}/\partial T)_C$ for the unsegregated boundary and as $-(\partial \Gamma_{gb}/\partial T)_{\Delta\mu}$ for the fully relaxed boundary [26, 27], where G_{gb} is the grain boundary Gibbs free energy. The grain boundary entropy has two major contributions: (i) vibrational entropy, $S_{gb,v}$ and (ii) configurational entropy, $S_{gb,c}$. Figure 3 shows the boundary vibrational entropy as a function of the grain boundary misorientation at several temperatures. In the case where segregation is not allowed [Fig. 3(a)], this plot is quite different from those describing the dependence on misorientation of the boundary free energy and first layer concentration. However, the misorientation dependence of the vibrational entropy in the unsegregated alloy is very similar to that found for pure gold [34]. A pronounced maximum occurs at $\theta = 28.07°$ (Σ17), a minimum appears at $\theta = 36.87°$ (Σ5) and an inflection occurs at $\theta = 22.62°$ (Σ13). The magnitude of the vibrational entropy increases with increasing temperature. In the segregated limit [Fig. 3(b)], the boundary vibrational entropy tends to vary smoothly with misorientation; no obvious inflection is observed. The effect of increasing temperature is to reduce the magnitude of the boundary vibrational entropy. This is because the vibrational entropy of Cu is larger than that of Ni [26, 27], therefore, as more Cu segregates to the boundary at lower temperature, a larger value of the vibrational entropy is expected. Note that the $S_{gb,v}$ vs θ curves are very similar to the total excess concentration $C_{T,xs}$ vs θ curves [Fig. 1(b)].

In the segregated boundary, the variation of the concentration on the boundary gives rise to another term in the entropy, the boundary configurational entropy $S_{gb,c}$, the misorientation dependence of which is shown in Fig. 4. The curves are quite smooth and no cusps are observed. The overall magnitude of $S_{gb,c}$ shows a complex variation with temperature. The values of the configurational entropy at $T = 600$ and 800 K decrease as the misorientation is increased, while for the higher temperatures examined, $S_{gb,c}$ increases as the misorientation increases. The temperature dependence of the $S_{gb,c}$ curves may be

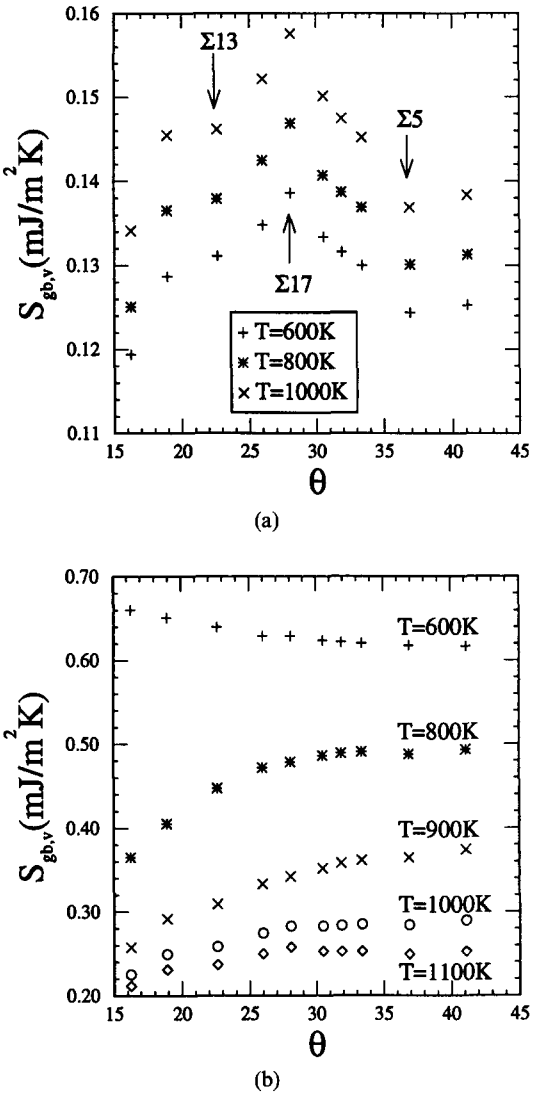

Fig. 3. The grain boundary vibrational entropy vs misorientation (a) for the unsegregated boundary and (b) for the segregated boundary.

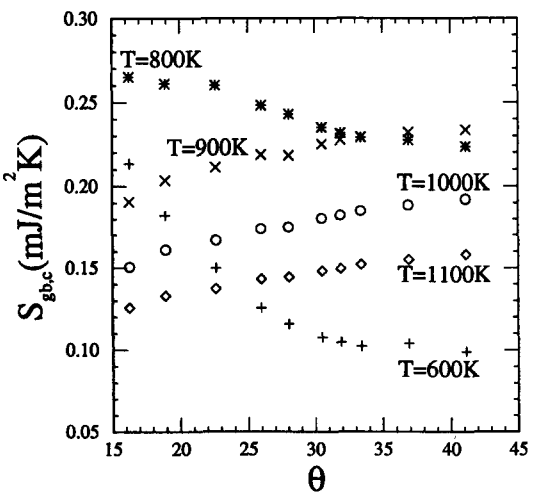

Fig. 4. The grain boundary configurational entropy vs grain boundary misorientation.

understood by considering the differences between S_c [equation (2)] calculated with $C = C_1$ (Fig. 1) and S_c calculated with $C = C_B$.

The grain boundary enthalpy H_{gb} was determined from $H_{gb} = G_{gb} + TS_{gb}$, where S_{gb} is the total grain boundary entropy, which is equal to $S_{gb,v}$ for unsegregated boundaries and $S_{gb,v} + S_{gb,c}$ for the segregated boundaries. The boundary enthalpy as a function of the misorientation is plotted in Fig. 5. For the unsegregated boundary, the boundary enthalpy generally increases with increasing misorientation, though a small local minimum is observed at Σ5. The effect of the temperature is to shift the curve to a slightly higher value. In the segregated case [Fig. 5(b)], the enthalpy also increases as the misorientation increases except at $T = 600$ K, for which H_{gb} slightly decreases as the misorientation increases. The dependence of the enthalpy on temperature is large when segregation is included, with the values at

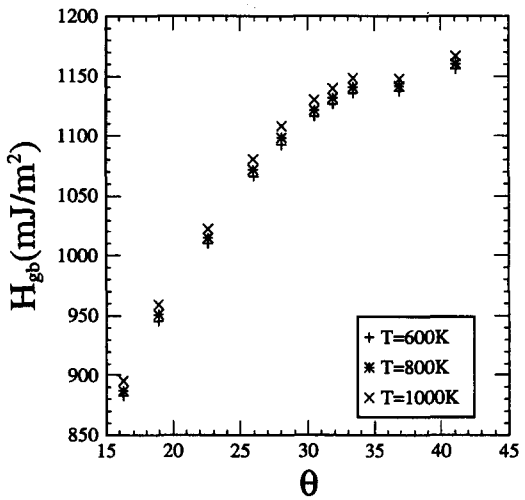

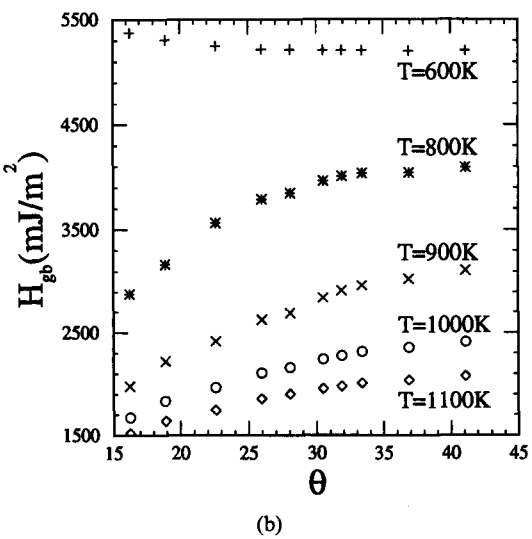

Fig. 5. The grain boundary enthalpy vs misorientation (a) for the unsegregated boundary and (b) for the segregated boundary.

$T = 600$ K being greater than at higher temperatures. Again, this is because pure Cu has a larger enthalpy than Ni [26, 27]; hence, as more Cu segregates to the boundary at lower temperatures, the grain boundary enthalpy increases. The H_{gb} vs θ curves are very similar to the boundary concentration $C_{T,xs}$ vs θ curves [Fig. 1(b)].

As described above, the two grains are allowed to move with respect to each other during the course of the relaxation. If the relative motion of the grains is parallel to the boundary plane, different boundary structures may result [8]. If the relative motion of the grains is perpendicular to the boundary plane, then the specific volume of the boundary increases. In practice, the boundary expansion (or the excess boundary volume) D_{gb} is measured as the *change* (relative to the perfect crystal at that temperature) in distance between two (002) planes (one in each grain) far from the boundary plane. The boundary expansion as a function of misorientation is plotted in Fig. 6. In the unsegregated case, the boundary expansion varies in a nearly linear manner with boundary misorientation. The effect of increasing temperature is to raise the magnitude of the expansion. For the segregated boundary, the boundary expansion monotonically increases as the misorientation increases and the effect of the temperature is to lower the magnitude of the boundary expansion. This is consistent with the fact that Cu atoms are larger than Ni atoms and that D_{gb} and $C_{T,xs}$ vs θ and T have very similar forms [compare Figs 1(b) and 6(b)]. The curves of the boundary properties, $S_{gb,v}$, H_{gb}, and D_{gb}, vs θ are very similar to that of $C_{T,xs}$ vs θ, which is consistent with the observation that these properties are linearly proportional to $C_{T,xs}$ in the $\Sigma 5$ boundary for a wide range of temperatures and bulk concentrations [26].

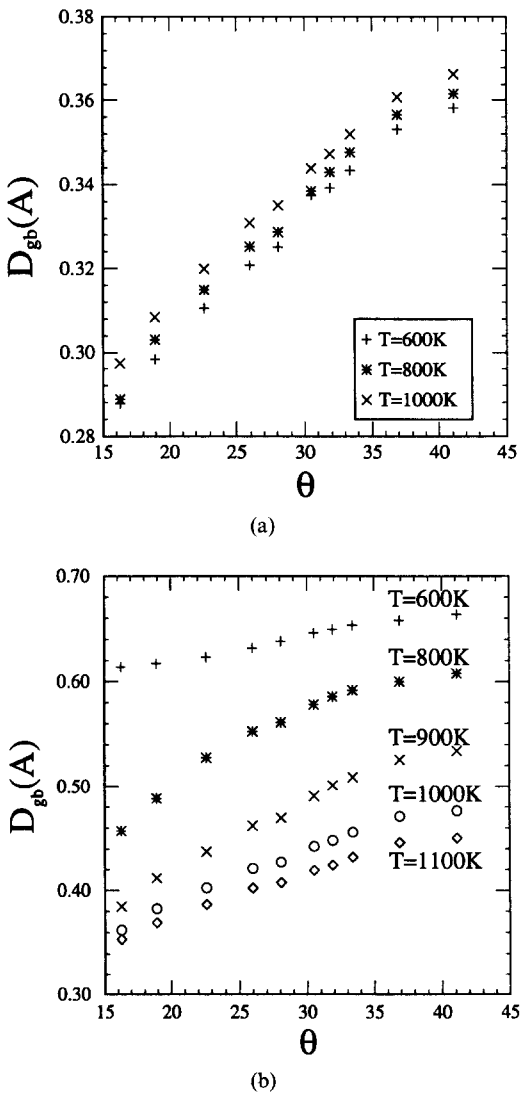

Fig. 6. The excess grain boundary volume vs misorientation (a) for the unsegregated boundary and (b) for the segregated boundary.

5. GRAIN BOUNDARY STRUCTURE

Following the notation of Schwartz *et al.* [15], the crystal units bounded by $\frac{1}{2}\langle 110\rangle$ and $\frac{1}{2}\langle 100\rangle$ in the perfect, ideal crystal appear in some (001) twist boundaries and are denoted as A and α units (see Fig. 7). The circles and squares in this figure represents two adjacent (002) planes. The two crystal units in the (001) $\Sigma 5$ twist boundary, bounded by $\frac{1}{2}\langle 310\rangle$ and $\frac{1}{2}\langle 210\rangle$, are denoted as B and β units (see the solid and dashed lines in Fig. 8, respectively). The circles and squares in this and the following figures represent the atoms from the (002) planes immediately above and below the grain boundary. The structural unit model describes the atomic structure of [001] twist boundaries as decompositions into a combination of A or α and B or β units, with the addition of filler units as needed. For misorientations

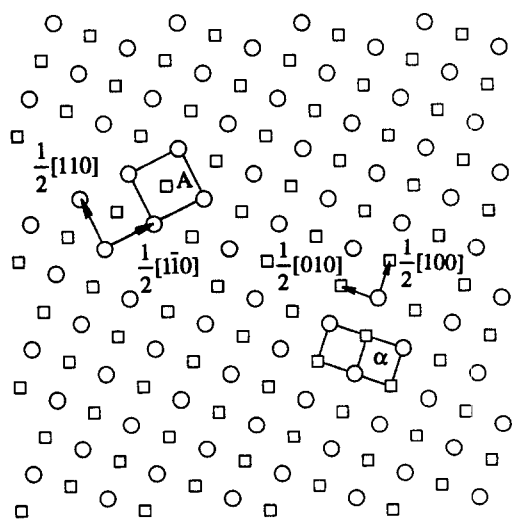

Fig. 7. Two (002) atomic planes of a perfect f.c.c. crystal denoted by the squares and circles respectively. Two unit cells A and α are identified. The area occupied by two α units is equal to that occupied by one A unit.

with angles less than 22.62° (Σ13), only one acceptable decomposition into units can be found, namely into [*A* plus *β*]. At misorientations greater than 22.62° but less than 36.87° (Σ5), there are always two different decompositions, [*A* plus *β*] and [*B* plus *α*]. When $36.87° \leqslant \theta \leqslant 45°$, the boundaries are composed of different units of the Σ5 boundary [*B* plus *β*] [15]. We observe that the same decomposition rules are also applicable to the segregated grain boundary structures. The different magnitude of the segregation from site to site creates a concentration pattern within the grain boundary and this pattern can be described within the same framework of the structural units model established by Schwartz *et al.* [15]. In the following sub-sections, owing to space limitations, we will examine the concentration distribution patterns for a subset of the simulated boundaries.

5.1. Σ5 (θ = 36.87°)

In Fig. 8, the Cu distribution within the planes on either side of the boundary is indicated. The gray level of each site indicates the magnitude of the average Cu concentration at that site. The darker gray levels correspond to larger Cu concentrations and the two extreme gray levels, black and white, represent the maximum and the minimum Cu concentration for that particular boundary. In the Σ5 boundary, only two different types of atomic sites are observed; these correspond to the coincidence lattice sites (CS) and non-coincidence lattice sites (NCS). The atomic environment around these two types of lattice sites is not the same; thus, the heat of segregation and concentration of segregant at each site is

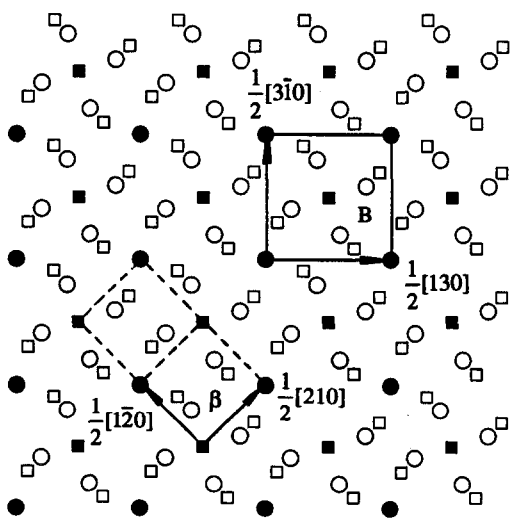

Fig. 8. The concentration distribution at the Σ5 boundary. Darker gray levels represent higher Cu concentrations. The squares and circles represent the effective atoms from the (002) atomic planes immediately above and below the boundary. Two unit cells *B* and *β* are identified: a *B* unit is delimited by solid lines and two *β* units by dashed lines. The concentrations at the black and the white sites are 0.8 and 0.65, respectively.

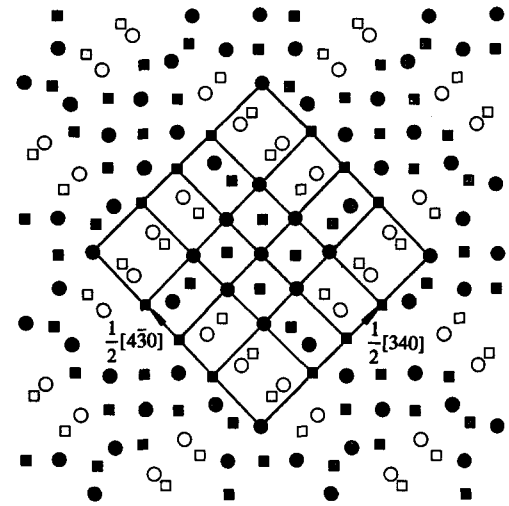

Fig. 9. The concentration distribution at the Σ25 boundary. Four *A* units are in the center, one *β* unit at each corner, and two filler units are on each side. The concentrations at the black and the white sites are 0.54 and 0.27, respectively.

different. The two site concentrations at this boundary, indicated by black and white symbols correspond to a Cu concentration of 0.8 and 0.65, respectively. The black sites are the CS's and the white sites are NCS's. Therefore CS's show stronger Cu segregation than do NCS's in this boundary.

The two unit cells, *B* (solid lines) and *β* (two cells are shown as dashed lines), are identified in Fig. 8. While *B* is a true unit cell in that it is periodically repeated within the structure, two *β* units must be taken together to form a true unit cell. However the two *β* units are related to each other by a 90° rotation about the center. The *β* units are known as "invariant" units that are bounded by the four twofold symmetry axes in the boundary. This notation is the same as that employed in Ref. [15]. The darker sites (CS) are located at the corners of *β* units and at the corner and center sites of *B* units. The white sites (NCS) are located within, but not at the center of, the *β* and *B* units.

5.2. Σ25 (θ = 16.26)

The concentration distribution at the Σ25 boundary is shown in Fig. 9, where the "invariant" unit cell is bounded by $\frac{1}{2}\langle 340\rangle$ directions. The outer solid lines in the figure include a slightly greater area than this invariant cell in order to make the symmetry more evident. The "invariant" unit cell consists of four *A* units (in the center), one *β* unit (one quarter of each of the four *β* units in the corners), and four filler units (one half of each of eight filler units between corner *β* units). Each of these units may be readily identified by comparison with Fig. 8 and the perfect crystal structure in Fig. 7. Each *A* (*β*) unit appears like all of the other *A* (*β*) units in terms of atomic arrangement and solute profile. In addition, the *A* and *β* units show essentially the same atomic arrangement as in the delimiting boundaries, i.e. the perfect crystal and

Σ5, respectively, which is in accordance with the structural unit model. Therefore, the structural unit model apparently works well even when boundary segregation occurs.

According to its symmetry, there are seven independent atomic sites in the Σ25 boundary. However, only four distinguishable concentration levels (indicated by black, white, dark gray, and light gray) can be observed in Fig. 9. The black atomic sites (53% Cu) are located at the corner of A units and β units; the white atomic sites (28%) are located within the β units; the dark gray sites (42%) are located within two of the filler units and the A units, and the light gray ones (37%) are located within the other two filler units. As in the concentration pattern of the Σ5 boundary (Fig. 8), the atomic sites in the β unit corresponding to the CS's (quasi-CS's) in the Σ5 boundary and have larger Cu concentration than the atomic sites (quasi-NCS's) corresponding to the NCS's in the Σ5 boundary. However, instead of showing uniform concentration as they would in the perfect crystal from which they are derived, the concentrations at the atomic sites in the A units have two distinct values, with the concentration in the corner sites being larger than that in the center. The largest site concentrations in the β units of the Σ25 boundary correspond to a much lower Cu concentration than the maximum concentration in the β units of the Σ5 boundary, which may be associated with the fact that the A and β units within this boundary are strained.

5.3. Σ13 ($\theta = 22.62°$)

The "invariant" unit cell of the Σ13 boundary is bounded by vectors of $\frac{1}{2}\langle 320\rangle$, which can be decomposed into $\frac{1}{2}\langle 110\rangle$ and $\frac{1}{2}\langle 210\rangle$, corresponding to a 1:1 mixture of A and β units. The concentration distribution is shown in Fig. 10 and, as before, a slightly larger unit cell is drawn to emphasize the symmetry. From the in-plane concentration distribution, one A unit (in the center), one β unit (in the corners), and two filler units (between two nearest neighbor β units) can be easily identified in the "invariant" unit cell of this boundary. Four distinct site concentrations and gray levels may be observed in Fig. 10, black (69% Cu) white (46%), dark gray (60%), and light gray (53%), with the black in the corner of the A or β units, the white within the β units, the dark gray within the A units, and the light gray within the filler units. The symmetry of the β unit is very similar to that in the Σ5 boundary except that the maximum concentration in the β units in the Σ13 boundary are significantly smaller than in the Σ5 delimiting boundary. These discrepancies between the basic units in the Σ13 boundary and those in the delimiting boundaries are also due to local strains in the boundary.

5.4. Σ17 ($\theta = 28.07°$)

The in-plane concentration profile associated with the Σ17 boundary is shown in Fig. 11. The invariant cell is bounded by $\frac{1}{2}\langle 140\rangle$. One B unit (see Fig. 8) of the Σ5 boundary (in the center) and one α unit (see Fig. 7) of the ideal crystal (in the corner) may be identified. There are only three different distinguishable concentration levels, white (51% Cu), black (71%), and gray (57%). The corners and the central five sites in the B unit are black, the four other atomic sites in the B unit are gray, and the ones within the filler units are white. The concentrations at the non-coincident sites in the B unit are not uniform, as they are in the Σ5 boundary, due to local strains. The discrepancy between the ideal B (Σ5) units and that in the Σ17 boundary is among the largest in any of

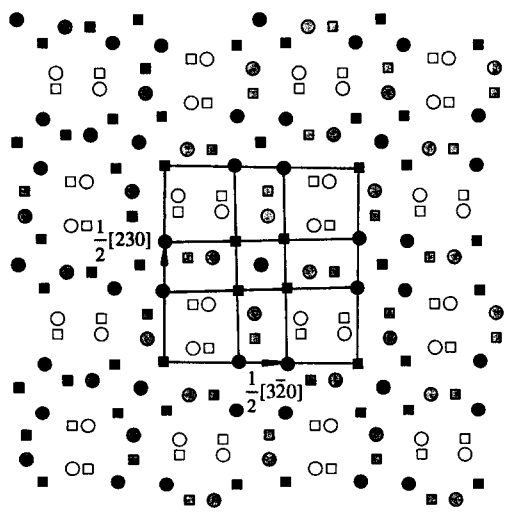

Fig. 10. The concentration distribution at the Σ13 boundary. One A unit is at the center, one β unit at each corner, and one filler unit is on each side. The concentrations at the black and the white sites are 0.69 and 0.46, respectively.

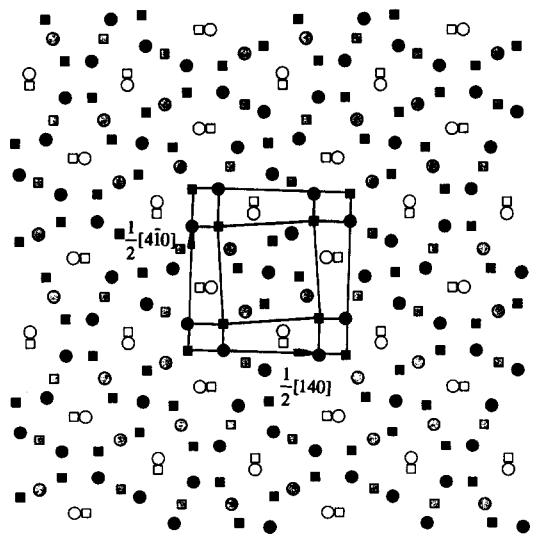

Fig. 11. The concentration distribution at the Σ17 boundary. One B unit is at the center, one α unit is at the corner, and one filler unit is on each side. The concentrations at the black and the white sites are 0.72 and 0.52, respectively.

the boundaries examined. Nonetheless, the decomposition of the boundary structure into structural units is still reasonable.

5.5. Σ109 (θ = 33.40°)

The concentration distribution pattern of the Σ109 boundary is shown in Fig. 12. The invariant cell is bounded by $\frac{1}{2}\langle 10, 3, 0\rangle$ and nine *B* units, one α unit (in the corners), and six filler units (between two nearest neighbor α units) may be identified in this cell. There should be 28 distinct atomic sites in the Σ109 boundary; however, only five clearly-distinct gray levels can be observed, black (79% Cu), white (59%), and three different gray levels (64%, 70% and 75%). The *B* units are somewhat distorted, but the gray level pattern is still very close to the one in the Σ5 boundary. Four distinct concentrations can be found in the *B* units, corresponding to black and three different gray levels, with the black sites in the corners and the center of the *B* units (the quasi-CS's) and the gray ones making up the remainder of the *B* units (the quasi-NCS's). Examination of the different *B* units suggest that the NCS's which are in this boundary show a large concentration variation within a given *B* unit and between *B* units, as compared with the pure *B* unit of the Σ5 in which all NCS's exhibit identical Cu concentrations. Within the filler units, there are two different shadings, white and one of the three different gray levels, with the white in two of the filler units and the gray in the other four.

5.6. Σ73 (θ = 41.11°)

As discussed above, when the misorientation is between 36.87° (Σ5) and 45°, the boundary is composed of two different Σ5 boundary structure units (the *B* and β units) and no *A* or α units. Such a decomposition rule is also applicable in the case when

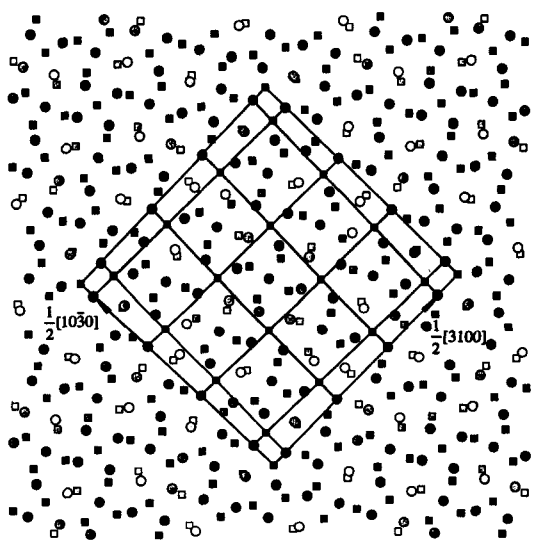

Fig. 12. The concentration distribution at the Σ109 boundary. Nine *B* units are at the center, one α unit is at the corner, and three filler units are on each side. The concentrations at the black and the white sites are 0.79 and 0.58, respectively.

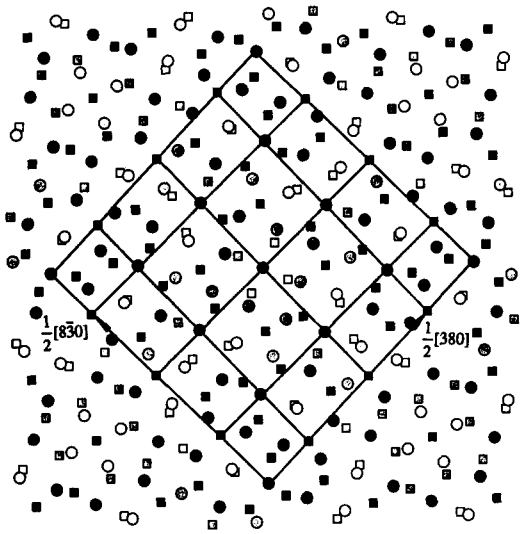

Fig. 13. The concentration distribution at the Σ73 boundary. Four *B* units are at the center, one β unit is in each corner, and two filler units are on each side. The concentrations at the black and the white sites are 0.82 and 0.61, respectively.

there is distribution of site concentrations. The Σ73 boundary (bounded by $\frac{1}{2}\langle 380\rangle$) is shown in Fig. 13, where four *B* units, one β unit (in the corners), and four filler units (between two nearest neighbor β units) can be identified. Five different gray levels may be identified, black (81% Cu), white (62%), dark gray (77%), medium gray (70%), and light gray (66%), which is far less than the number of possible distinct atomic sites, 19. The shading of the quasi-CS's sites in the *B* and β units is black and the atomic sites within the β units (quasi-NCS's) uniformly exhibit the same dark gray level. However, in the *B* unit, the quasi-NCS's exhibit two distinct shadings, light gray and white, which is due to the strains within these units. The filler units exhibit three distinct gray levels.

5.7. General structural observations

As discussed above, the atomic positions in the [001] twist grain boundaries can be described within the structural unit model framework that was established for grain boundary structures of pure materials over a wide range of misorientation. However, the *A*, α, *B* and β unit structures identified in the boundaries show some distortion with respect to the same units in the delimiting boundaries. The segregation to the atomic sites within these units is quite sensitive to such distortion and thus we find considerable variation in the concentration pattens in the unit structures as a function of misorientation. Nonetheless, segregation does not destroy the basic features of the structural unit model and the decomposition of the boundary into distinct units is still reasonable. The number of the distinct site concentrations, in most cases examined, is less than the number of possible distinct atomic sites in the boundary.

6. HYDROSTATIC STRESS

In Fig. 14(a–c), we show the hydrostatic stress, defined as $p_i = \frac{1}{3}(\sigma^i_{11} + \sigma^i_{22} + \sigma^i_{33})$, at each site on the (002) planes immediately adjacent to the Σ5, Σ13, and Σ109 boundaries in the absence of segregation. The atomic-level stress tensor $\sigma^i_{\alpha\beta}$ is evaluated as [35]

$$\sigma^i_{\alpha\beta} = \frac{1}{2v_i}\sum_j \left(\frac{\partial G}{\partial r_{ij}}\right)\frac{r^\alpha_{ij} r^\beta_{ij}}{r_{ij}} \tag{4}$$

where G is the Gibbs free energy, v_i is the volume ascribed to atom i, r_{ij} is the distance between site i and site j, and r^α_{ij} and r^β_{ij} are the α and β components of the vector $\mathbf{r}_{ij}$ separating atoms i and j, the summation

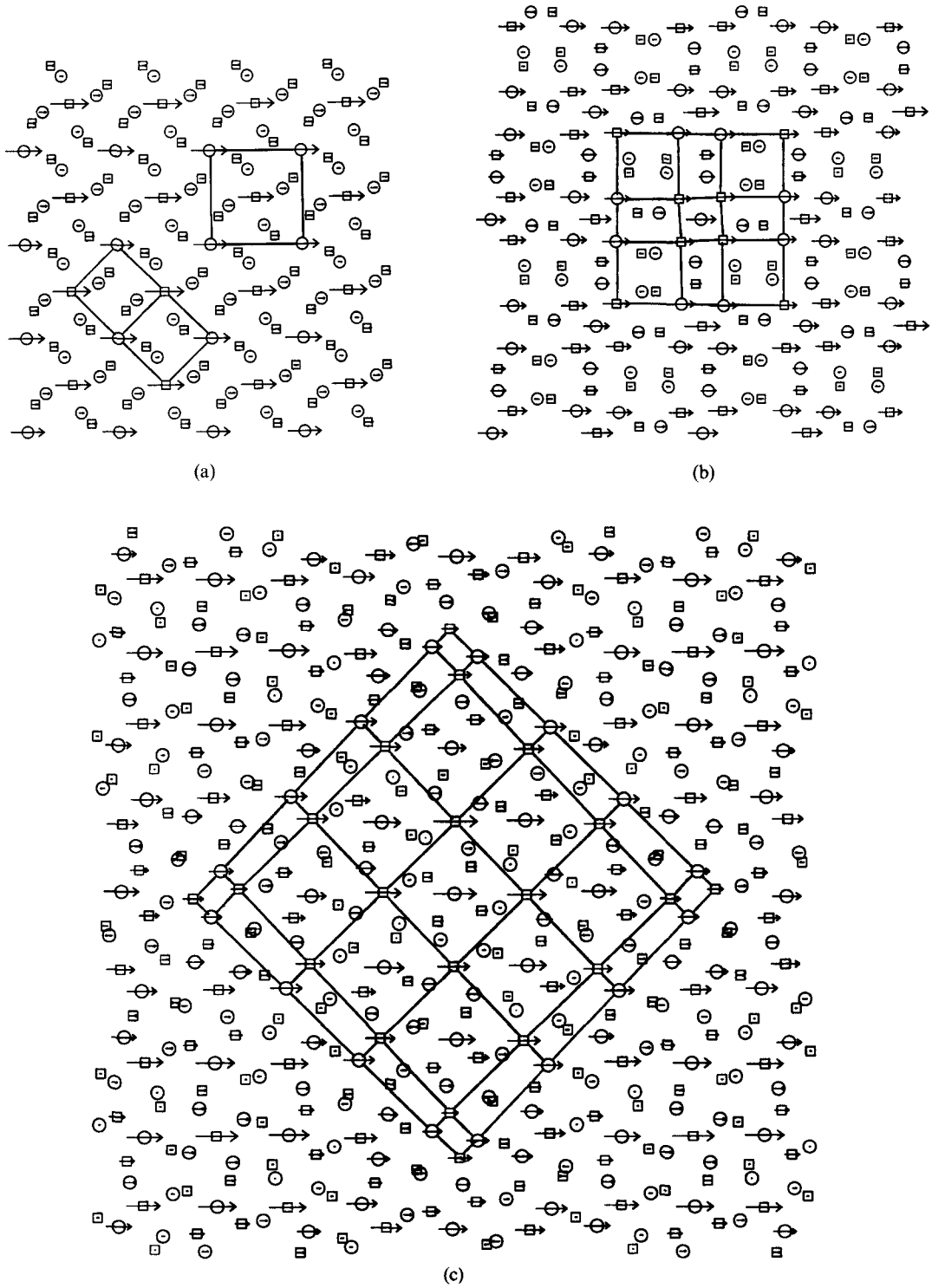

Fig. 14. Maps of the hydrostatic stress before segregation at the (a) Σ5, (b) Σ13 and (c) Σ109 boundaries.

is over all of the neighbors of site i. In a perfect, primitive crystal, the p_i do not vary from site to site and are all equal to the external pressure. In Fig. 14, the hydrostatic stress is represented by an arrow centered at the atom site, the length of which is proportional to its magnitude. Arrows pointing to the right correspond to a positive stress (tension) and those to the left to a negative stress (compression).

The hydrostatic stress at the CS's of the Σ5 boundary before segregation [Fig. 14(a)] is much larger than that at the NCS's and both sites are under tension. In the unsegregated Σ13 and Σ109 boundaries [Fig. 14(b,c)], the quasi-CS's in the β and B units and the atomic sites in the A and α units have much larger hydrostatic stresses than do the other atomic sites. Comparing these results with the in-plane concentration distributions at the same boundaries

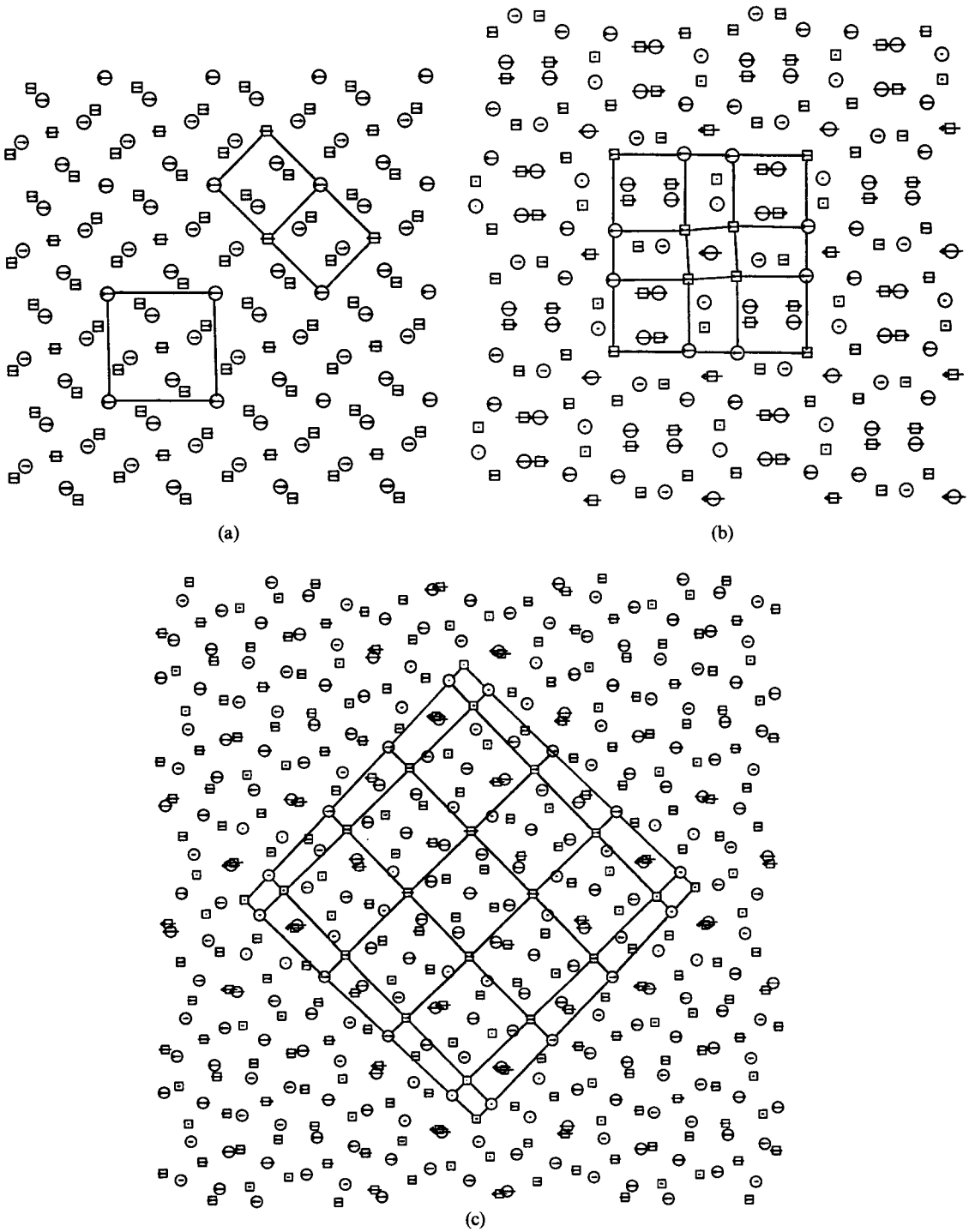

Fig. 15. Maps of the hydrostatic stress after segregation at the (a) Σ5, (b) Σ13 and (c) Σ109 boundaries.

(Figs 8, 10 and 12), we find that the atomic sites with large tensile stresses in the unsegregated boundaries exhibit a very much enhanced Cu concentration when segregation occurs. Indeed, in the Σ13 and Σ109 boundaries, the white sites are under compressive rather than tensile stresses and show only very small increases in Cu concentration upon segregation.

The hydrostatic stresses were also determined after segregation for the Σ5, Σ13 and Σ109 boundaries [Fig. 15(a–c)]. In each case, the magnitude of the stresses is greatly reduced by Cu segregation. In the Σ5 boundary, for example, the strong pre-segregation hydrostatic stresses at the CS's [Figs 14(a) and 15(a)] are greatly reduced upon segregation and the minimum stress, which occurred at the NCS's before segregation, changes from tension to slight compression. Essentially the same observation hold for the Σ13 and Σ109 boundaries [Fig. 15(b,c)], where the maximum hydrostatic stresses in both the Σ13 and Σ109 boundaries are drastically reduced. Some of the smaller tensile stresses become compressive and the magnitude of the compressive stresses increases by a small amount upon segregation.

The reduction of the tensile hydrostatic stresses upon segregation is associated with the larger size of Cu relative to Ni. When Cu segregates to the boundary, the larger Cu fills the "holes", "free volume" or extended regions in the boundary structure, thereby reducing the tensile stress. The site-to-site variation in the hydrostatic stress within the boundary is greatly reduced because segregation occurs to a much greater degree where the hydrostatic tension is larger. The reduction of the maximum hydrostatic stress because of segregation is observed for all of the boundaries examined.

7. SHEAR STRESS

The atomic-level shear stress associated with atom i may be evaluated as $\tau_i = \sqrt{(\sigma^i_{13})^2 + (\sigma^i_{23})^2}$, where the 3 direction is chosen to be normal to the boundary plane. The map of the shear stress field of the Σ25 boundary before and after segregation is shown in Fig. 16(a) and (b), respectively, where the shear stresses are indicated by arrows with magnitude and direction given by the vector $\tau_i = (\sigma^i_{13}, \sigma^i_{23})$. The largest shear stresses in the unsegregated boundary plane [Fig. 16(a)] occur near the points where the screw dislocations (GBD) that make up the grain boundary intersect. The positions of the screw dislocations are indicated by the solid lines in Fig. 16. Comparison of this figure with the structural unit figure shown in Fig. 9 demonstrates that the dislocations are centered at the filler units and intersect at the β units. The inter-dislocation regions correspond to the majority A units. The magnitude of the shear stress is larger at the cores of dislocations than in the inter-dislocation A units and the largest shear stresses occur in the β units.

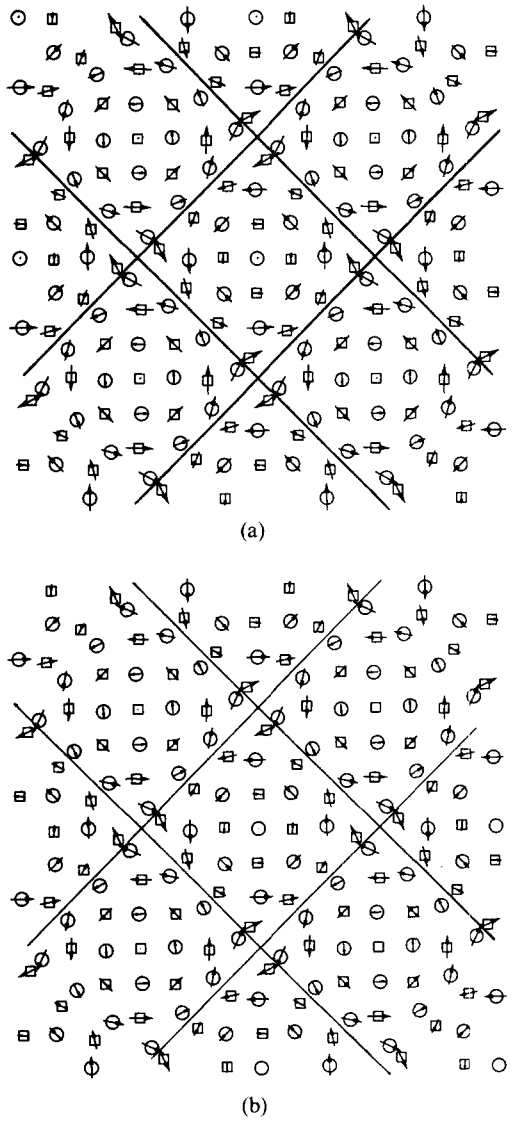

Fig. 16. Maps of the shear stress at the (a) for the unsegregated and (b) segregated Σ25 boundary.

After segregation [Fig. 16(b)], the overall magnitudes of the shear stresses are reduced, but only by a small amount (much less than in the case of the hydrostatic stresses). Therefore, we must conclude that the effect of the segregation on the shear stresses at the boundary are relatively insignificant. This same observation may be made with respect to all of the boundaries examined in the present study. Unlike the hydrostatic stresses, which depend on the local volume or density, the shear stresses are more closely related to the symmetry of the atomic sites in the boundary plane, which, as demonstrated above, are relatively unchanged upon segregation.

8. SUMMARY

We have investigated the segregation, thermodynamic, and structural properties of [001] twist boundaries in the solid solution alloy $Ni_{1-x}Cu_x$,

with $x = 0.05$, within the misorientation range $15° \leqslant \theta \leqslant 45°$ at temperatures $600\,K \leqslant T \leqslant 1100\,K$. The results show that Cu segregates to the boundary for all misorientation angles and temperatures studied. The average Cu concentration on the first (002) atomic plane adjacent to the boundary increases monotonically with misorientation and no strong cusps are observed. Except for the vibrational entropy in the unsegregated boundaries, all of the thermodynamic properties vary smoothly with misorientation in a manner very similar to the misorientation-dependent boundary Cu concentration. The unsegregated vibrational entropy is quite distinct; it shows a large peak around the $\Sigma 17$ boundary and two minima around the $\Sigma 13$ and $\Sigma 5$ boundaries. The distribution of site concentrations at the grain boundaries exhibits a pattern that can be described in terms of the same structural unit model established for the structure of [001] twist boundaries in pure materials. The concentration distribution pattern of the boundaries with misorientations less than 36.87° ($\Sigma 5$) can be decomposed into units of ideal crystals, units of $\Sigma 5$ boundary, and filler units, while the concentration distributions pattern of the boundaries with misorientations between 36.87° and 45° consist of different $\Sigma 5$ boundary units and filler units. Although the segregant distribution within individual structural units shows large variations within a boundary and between boundaries composed of the same units, the structural unit model still provides a good description of the atomic structure of the segregated boundaries. The atomic-level hydrostatic and shear stresses were also determined. Atomic sites with large hydrostatic tensile stresses before segregation are the sites to which the greatest degree of Cu segregation occurs. After segregation, the maximum hydrostatic stress is reduced so significantly that the magnitude of the stress on all sites is very similar. While there is some reduction in atomic level shear stresses upon segregation, this effect is weak. These effects seem to be associated with the larger size of the Cu atoms relative to Ni atoms and hence Cu segregation reduces the hydrostatic tension. The shear stresses depend predominantly on the local symmetry, which is only slightly modified by segregation.

REFERENCES

1. P. J. Goodhew, in *Grain Boundary Structure and Kinetics* (edited by R. W. Balluffi), Soc. Metals, Metal Park, Ohio (1980).
2. R. Maurer, *Acta metall.* **35,** 2557 (1987).
3. H. Sautter, H. Gleiter and G. Baro, *Acta metall.* **25,** 467 (1977).
4. A. P. Sutton and R. W. Balluffi, *Acta metall.* **35,** 2177 (1987).
5. H. F. Fischmeister, *J. Phys.* **46** (Suppl.), C4-3 (1985).
6. G. J. Wang and V. Vitek, *Acta metall.* **34,** 951 (1986).
7. J. Th. M. De Hosson and V. Vitek, *Phil. Mag. A* **61,** 305 (1990).
8. R. Najafabadi, D. J. Srolovitz and R. Le Sar, *J. Mater. Res.* **6,** 999 (1991).
9. *Proc. Interface Science and Engineering '87* (edited by R. Raj and S. Sass), *J. Physique* **49,** C5 (1988).
10. V. Pontikis, *J. Physique* **47,** C5-327 (1988).
11. A. P. Sutton, Ph. D. thesis, Univ. of Pensylvania (1981).
12. A. P. Sutton, *Phil. Mag. A* **64,** 171 (1982).
13. A. P. Sutton and V. Vitek, *Phil. Trans. R. Soc. Lond. A* **309,** 1 (1983); 37 (1983); 55 (1983).
14. G. J. Wang, A. P. Sutton and V. Vitek, *Acta metall.* **32,** 1093 (1984).
15. D. Schwartz, V. Vitek and A. P. Sutton, *Phil. Mag. A* **51,** 499 (1985).
16. R. W. Balluffi and P. D. Bristowe, *Surf. Sci.* **144,** 28 (1984).
17. R. W. Baluffi and P. D. Bristowe, *J. Phys.* **46,** C4-155 (1985).
18. G. J. Wang and V. Vitek, *J. Physique* **43,** C6-147 (1982).
19. D. MacLean, *Grain Boundaries in Metals.* Oxford Univ. Press, Oxford (1957).
20. S. M. Foiles, *Phys. Rev. B* **32,** 7685 (1985).
21. S. M. Foiles, *Phys. Rev. B* **40,** 11502 (1989).
22. P. Bacher, P. Wynblatt and S. M. Foiles, *Acta metall. mater.* **39,** 2681 (1991).
23. S. M. Kuo, A. Seki, Y. Oh and D. N. Seidman, *Phys. Rev. Lett.* **65,** 199 (1990).
24. R. Najafabadi, H. Y. Wang, D. J. Srolovitz and R. LeSar, *Acta metall. mater.* **39,** 3071 (1991).
25. H. Y. Wang, R. Najafabadi, D. J. Srolovitz and R. LeSar, *Mater. Res. Soc. Symp. Proc.* **209,** 219 (1991).
26. H. Y. Wang, R. Najafabadi, D. J. Srolovitz and R. LeSar, *Phil. Mag. A* **65,** 625 (1992).
27. H. Y. Wang, R. Najafabadi, D. J. Srolovitz and R. LeSar, *Phys. Rev. B* **45,** 12028 (1992).
28. H. Y. Wang, R. Najafabadi, D. J. Srolovitz and R. LeSar, *Phys. Rev.*, submitted.
29. H. Y. Wang, R. Najafabadi, D. J. Srolovitz and R. LeSar, *Phys. Rev.*, submitted.
30. R. LeSar, R. Najafabadi and D. J. Srolovitz, *Phys. Rev. Lett.* **63,** 624 (1989).
31. W. L. Bragg and E. J. Williams, *Proc. R. Soc. A* **145,** 699 (1935); **151,** 50 (1935).
32. K. Huang, *Statistical Mechanics.* Wiley, New York (1963).
33. M. Lundberg, *Phys. Rev. B* **36,** 4692 (1987).
34. R. Najafabadi, D. J. Srolovitz and R. LeSar, *J. Mater. Res.* **5,** 2663 (1990).
35. M. Born and K. Huang, *Dynamical Theory of Crystal Lattice*, p. 245. Oxford Univ. Press, Cambridge (1954).
36. L. Zhao, R. Najafabadi and D. J. Srolovitz, *Modeling and Simulation in Material Science and Engineering*, in press.
37. R. LeSar, R. Najafabadi and H. Y. Wang, unpublished.
38. L. Zhao, R. Najafabadi and D. J. Srolovitz, to be published.